

# What Sets Temperature Gradients in Galaxy Clusters? Implications for non-thermal pressure support and mass-observable scaling relations.

Michael McCourt,<sup>1\*</sup> Eliot Quataert,<sup>1</sup> & Ian J. Parrish<sup>1,2</sup>

<sup>1</sup>*Department of Astronomy and Theoretical Astrophysics Center, University of California Berkeley, Berkeley, CA 94720*

<sup>2</sup>*Present address: Canadian Institute for Theoretical Astrophysics, 60 St. George Street, University of Toronto, Toronto, ON M5S 3H8, Canada*

Submitted to MNRAS, December 2012

## ABSTRACT

We present a spherically symmetric model for the origin and evolution of the temperature profiles in the hot plasma filling galaxy groups and clusters. We find that the gas in clusters is generically not isothermal, and that the temperature declines with radius at large distances from the cluster center (outside the core- and scale radii). This temperature profile is determined by the accretion history of the halo, and is not quantitatively well-described by a polytropic model. We explain quantitatively how the large-scale temperature gradient persists in spite of thermal conduction and convection. These results are a consequence of the cosmological assembly of clusters and cannot be reproduced with non-cosmological simulations of isolated halos. We show that the variation in halo assembly histories produces a  $\sim 10\%$  scatter in temperature at fixed mass. On top of this scatter, conduction decreases the temperature of the gas near the scale radius in massive clusters, which may bias hydrostatic mass estimates inferred from x-ray and SZ observations. As an example application of our model profiles, we use mixing-length theory to estimate the turbulent pressure support created by the magnetothermal instability (MTI): in agreement with our earlier MHD simulations, we find that the convection produced by the MTI can provide  $\sim 5\%$  non-thermal pressure support near  $r_{500}$ . The magnitude of this turbulent pressure support is likely to be non-monotonic in halo mass, peaking in  $\sim 10^{14.5} M_{\odot}$  halos.

**Key words:** galaxies: evolution, galaxies: halos, galaxies: clusters: intracluster medium

## 1 INTRODUCTION

X-ray observations of the hot, diffuse gas in galaxy groups and clusters suggest negative temperature gradients at large radii (Leccardi & Molendi 2008; George et al. 2009; Simionescu et al. 2011). This observation is somewhat surprising because negative temperature gradients are susceptible to a convective instability known as the magnetothermal instability, or MTI (Balbus 2001). Without a clear source of free energy to maintain the convection, it seems unusual that clusters should so uniformly be found in unstable states. This observation becomes even more surprising in clusters more massive than  $\sim 10^{14.5} M_{\odot}$ , where the timescale for heat to diffuse through the ICM can be much shorter than the Hubble time. Left to

their own devices, both conduction and convection tend to erase temperature gradients, and one might expect them to make the gas isothermal. In this paper, we study how the assembly of clusters creates large-scale temperature gradients and maintains them in spite of convection and thermal conduction.

Our subject is not purely academic. Systematic trends in temperature gradients with mass and redshift may influence the conversion of observable quantities (such as the x-ray surface brightness) to thermodynamic quantities (gas density, pressure, etc.). Understanding the origin of the temperature gradients in clusters would also enable us to calculate how the turbulence produced by the MTI depends on halo mass or redshift. These trends create systematic variations in non-thermal pressure support and might affect current efforts to use the cluster mass function to constrain cosmology (Allen

\* E-mail: mkmcc@astro.berkeley.edu

et al. 2008; Shaw et al. 2010; Allen et al. 2011). Thus, while the temperature profiles in galaxy clusters present an interesting puzzle in their own right, understanding the processes which control them may also find useful application in cluster cosmology.

Several studies, including Dolag et al. (2004), Burns et al. (2010), and Ruszkowski et al. (2011) have begun to address the effects of conduction and the MTI in the ICM using cosmological simulations. These results are computationally expensive, however, and can be difficult to interpret. For example, the MTI is expected to be a sub-dominant, but significant, source of turbulence in clusters (cf. Lau et al. 2009 and Parrish et al. 2012). Using cosmological simulations to study its trends with mass and redshift would require very careful calibration of other sources of turbulence. Thus, we feel that a simplified treatment which affords an intuitive understanding of the results remains useful.

The temperature and entropy profiles in the ICM are related by hydrostatic equilibrium. Accordingly, this paper closely follows earlier work by Tozzi & Norman (2001) and Voit et al. (2003), who study the entropy profiles in clusters. However, the processes controlling temperature gradients in clusters are slightly more subtle than those which determine their entropy profiles. Radial variations in entropy tend to be much larger than those in temperature, so small differences in the entropy profiles translate to much larger differences in temperature profiles. For the same reason, thermal conduction has a more pronounced effect on the temperature profile than on entropy and we must include it in our analysis. Thus, despite significant similarities to both Tozzi & Norman (2001) and Voit et al. (2003), our models represent a generalization of these earlier studies and we use them to explore different astrophysical applications. Komatsu & Seljak (2001) also present analytic models for temperature profiles in clusters. As we describe below, however, our method differs significantly from theirs because we do not assume a polytropic model for the gas; instead we directly calculate its thermodynamic state.

We describe our general methodology in the next section, followed by two sets of models. We begin in section 3 with an idealized but intuitive model. This section illustrates the key process that sets temperature gradients in clusters, but is too idealized to be directly compared with real clusters. We generalize this model in section 4 to more accurately reflect the formation histories and gravitational potentials of clusters. We also study the influence of thermal conduction on our results. We close in § 5 with a brief summary of our conclusions and a description of our future plans to apply them to observations and to more realistic simulations.

## 2 METHOD

Following Tozzi & Norman (2001) and Voit et al. (2003) (hereafter V03), we model the cosmological assembly of a galaxy cluster and use the evolving properties of its accretion shock to calculate the thermal state of the gas in its ICM. Then, by assuming the ICM is in hydrostatic equilibrium, we determine its temperature and pressure profiles. We focus our attention

on how the accretion history of a halo influences its temperature profile, and on how this temperature profile is later modified by thermal conduction. As discussed in section 1, we build on previous work that has focused on cluster entropy profiles.

Since the dynamical timescale in clusters is typically shorter than the timescales for either accretion or thermal conduction, we approximate the dynamics of the gas by assuming that it is in hydrostatic equilibrium at all times. We note that this assumption of strict hydrostatic equilibrium within the virial shock is not quantitatively justified: cosmological simulations of cluster formation (e. g. Rasia et al. 2006; Nagai et al. 2007; Lau et al. 2009; Vazza et al. 2011) consistently find  $\sim 10\text{--}20\%$  turbulent pressure support driven by mergers near the virial radius. Our assumption of hydrostatic equilibrium represents a first approximation and provides a simple model with no free parameters.

Our assumption of spherical symmetry is also an approximation: galaxy cluster halos are tri-axial and grow partly by accreting smaller sub-halos. The extent to which these properties influence the temperature profiles in clusters is not entirely clear; including them in our analysis would require cosmological simulations, however, and would likely obscure our results. Instead, we model clusters as spherically symmetric and we assume that they grow primarily via smooth accretion. Though these approximations are not entirely realistic, they are partially justified in V03, who compare models based on smooth accretion with more realistic ones based on hierarchical structure formation: the differences are modest for high-mass halos and mostly reflect changes in normalization due to clumping factors.

Each shell of material accreted by the cluster contains both dark and baryonic matter. We do not solve for the evolution of the dark matter; instead, we assume that the dark matter virializes rapidly and we parametrize it with a time-dependent fit to the potential (we neglect the gravity due to the baryons). We consider both simplified, isothermal potentials (§ 3) and more realistic fits to cosmological simulations (§ 4).

The baryons enter the cluster through a shock with a density  $\rho_{b,i}$  and velocity  $v_i$  determined by the accretion rate and by the depth of the potential:

$$\rho_{b,i} v_i = \frac{f_b}{4\pi} \frac{1}{r_{sh}^2} \frac{\partial M_{sh}}{\partial t}$$

$$v_i^2 = \frac{2GM_{sh}}{r_{sh}} (1 - \xi).$$

In the above,  $r_{sh}$  is the radius of the accretion shock,  $M_{sh}$  is the total mass contained within it, and  $f_b \approx 0.17$  is the cosmic baryon fraction. The parameter  $\xi = r_{sh}/r_{ta}$  parametrizes the strength of the virial shock, and  $r_{ta}$  is the “turnaround” radius, at which the kinetic energy of the shell vanishes (Gunn & Gott 1972).<sup>1</sup> We assume that the IGM is cold enough that

<sup>1</sup> Note that identifying  $\xi$  with  $r_{sh}/r_{ta}$  assumes that the baryons do not separate from dark matter before reaching the virial shock. If this were not the case, the baryons would feel a time-dependent potential due to the dark matter. Tozzi & Norman (2001) find that this may introduce a  $\sim 10\%$  correction to the infall velocity.

the gas enters the cluster through a strong shock (with an upstream Mach number  $M \gg 1$ ). Thus, the post-shock density and pressure are given by:

$$P_{\text{sh}} = \frac{3}{4} \rho_{\text{b},i} \left( \frac{4}{3} v_i \right)^2$$

$$\rho_{\text{sh}} = 4 \rho_{\text{b},i},$$

where the factor of  $4/3$  in front of the velocity transforms the infall velocity from the frame of the cluster to the frame of the shock. Thus, the post-shock entropy ( $K \equiv k_B T n^{-2/3}$ ) is:

$$K_{\text{sh}} = \frac{1}{3} \left( \frac{f_b}{4\pi} \right)^{-2/3} \left[ \frac{G^4 M_{\text{sh}}^2 (\mu m_p)^5}{\left( \frac{\partial \ln M_{\text{sh}}}{\partial t} \right)^2} (1 - \xi)^4 \right]^{1/3}. \quad (1)$$

Equation 1, above, is identical to equation 8 in V03. As emphasized in V03, apart from an overall normalization  $\propto (M/f_b)^{2/3}$ , the entropy profile depends only on the accretion history and on the shock strength  $\xi$ .

The jump conditions above represent the conservation of mass, momentum, and energy and thus reflect the *total* pressure behind the shock. In general, however, the electron and ion pressures may differ. The difference may be significant in clusters because the shock preferentially heats ions and because the timescale for electrons and ions to equilibrate is long (Fox & Loeb 1997). We don't distinguish between electron and ion temperatures in our calculation because the temperature difference does not effect hydrostatic equilibrium and thus should not influence our solutions. Moreover, the simulations by Rudd & Nagai (2009) show that this temperature difference is modest within the virial radius of the cluster.

Our assumption of a strong virial shock may not be valid for the innermost shells of material, which accreted when the IGM was hotter, and when the gravitational potential of the halo was shallower, than they are today. Hence, our model will not accurately reproduce the gas profiles near the centers of clusters (Tozzi & Norman 2001). Many other processes, including cooling, heating, and the formation of the central galaxy also affect the structure of the core, however (Voit 2011). We instead focus on the gas at larger radii, near the virial radius. Both the large mass and the long cooling time of this gas enable us to ignore galaxy formation processes at smaller radii (e.g. Voit & Ponman 2003; Voit 2011).

After undergoing the virial shock, the gas entropy evolves due to thermal conduction. Thermal conduction is highly anisotropic in the ICM because the electron mean free path is much longer than its gyroradius. Anisotropic conduction renders the ICM unstable to the MTI (Balbus 2001), however, which generates turbulence and may isotropize the magnetic field (McCourt et al. 2011; Parrish et al. 2012). We therefore parametrize thermal conduction through an effective isotropic conductivity. We introduce the effective conductivity  $\kappa_{\text{eff}} \equiv f_{\text{Sp}} \kappa_e$ , where  $f_{\text{Sp}} \sim 1/3$  is a suppression factor due to the magnetic field.<sup>2</sup> Thus, the evolution of the entropy

is determined by the following energy equation:

$$\frac{d}{dt} \ln K = \frac{2}{3P} \nabla \cdot \left( \frac{\kappa_{\text{eff}}}{k_B} \nabla T \right). \quad (2)$$

In the simplifying case that  $\kappa_{\text{eff}} \rightarrow 0$ , the entropy of each shell is a constant in time and equal to  $K_{\text{sh}}$ , given by equation 1. In addition to the conductivity  $\kappa$ , we also use the thermal diffusion coefficient  $\chi_e \equiv \kappa_e / (n_e k_B)$ , which has units of  $\text{cm}^2/\text{s}$ .

As mentioned above, anisotropic thermal conduction in the ICM drives a convective instability known as the MTI. This convection carries a heat flux which should technically be added to equation 2. However, the convective heat flux is smaller than the conductive flux by a factor of

$$\frac{Q_{\text{conv}}}{Q_{\text{cond}}} \sim \sqrt{\frac{m_e}{m_i}} \left( \frac{H}{\lambda_e} \right) \alpha^3 \left( H \frac{d \ln T}{dr} \right)^{3/2},$$

where  $m_e$  and  $m_i$  are the electron and ion masses,  $H$  is the pressure scale-height,  $\lambda_e$  is the electron mean-free-path, and  $\alpha$  is the mixing-length parameter of the convection. This ratio is small ( $\sim 10^{-2}$ ) in the ICM, enabling us to ignore the convective heat flux in equation 2 (cf. Parrish et al. 2008).

Our spherically symmetric model is most easily represented in Lagrangian coordinates with the enclosed mass as the independent variable. Thus, the continuity equation and the equation for hydrostatic equilibrium take the form:

$$\mu m_p \frac{dr}{dM_b} = \frac{1}{4\pi r^2} \left( \frac{K}{P} \right)^{3/5}, \quad (3)$$

$$\frac{dP}{dM_b} = -\frac{g}{4\pi r^2}, \quad (4)$$

where  $M_b$  is the *baryonic* mass contained within the radius  $r$ , and we adopt the entropy  $K$  and pressure  $P$  as our primary thermodynamic variables. In this initial study, we ignore sources of non-thermal pressure support (such as cosmic rays, magnetic fields, or turbulence). However, we discuss in section 5 our plans to self-consistently include turbulence generated by the MTI and to compare these results with cosmological simulations.

Equations 1–4 completely specify our model except for the mass accretion history  $M_{\text{sh}}(t)$  and the gravitational field  $g(r, t)$  of the halo. We assume that these are determined by cosmology and are unaffected by the baryonic formation of the cluster. We describe a simple, idealized model for the halo formation in section 3 and a more realistic model in section 4.

### 3 SIMPLIFIED ADIABATIC MODELS

Before studying the consequences of thermal conduction, it is useful to understand the ‘baseline’ temperature profile generated by the halo’s mass accretion history. Thus, we begin with adiabatic models which ignore thermal conduction. We further isolate the influence of the accretion history by assuming the gravitational potential is isothermal and that the accretion rate of the cluster is independent of time:

<sup>2</sup> Though this approximation is suitable for our purposes, we note in passing that the use of an isotropic conductivity significantly alters other processes in the ICM, such as convection (Balbus 2001; Quataert 2008) and thermal instability (Sharma et al. 2010; Mc-

Court et al. 2012; Sharma et al. 2012), and is thus not suitable for more detailed dynamical studies. Interestingly, a suppression factor  $f_{\text{Sp}} \sim 1/3$  turns out to be appropriate even if the magnetic field is tangled on very small scales (Narayan & Medvedev 2001).

$M_{\text{sh}}(t) = M_0 \times t/t_0$ . As we show later, this prescription contains only a single free parameter and is perhaps the simplest nontrivial model of the process we wish to study. Though the results in this section cannot be directly applied to clusters, they highlight some of the key physics determining the temperature gradients in clusters, and will assist in our interpretation of the more detailed models in section 4.

The next step in our model is to determine the shock strength  $\xi$ . The most logical choice would be to calculate  $\xi(M_b)$  so that the cluster was in hydrostatic equilibrium at every epoch; in fact, this is formally required to use equation 1 for the post-shock entropy. In this section, however, we make the simplifying assumption that  $\xi(M_b)$  is a constant. Thus, the models presented in this section are not entirely self-consistent. Our goal in this section is only to obtain an intuitive understanding of how the accretion rate of a halo influences its temperature gradient. We present more detailed models, with more accurate results, in section 4.

Since we have assumed a solution for  $\xi(M_b)$  and that the evolution of the gas is adiabatic, the entropy profile  $K(M_b)$  is uniquely determined at all times by equation 1. Thus, it suffices to solve hydrostatic equilibrium only at the present epoch – this solution cannot depend on the state of the cluster at earlier times. Hence, we need not track the evolution of the cluster, and the equations determining the state of the gas reduce to ordinary differential equations.

### 3.1 Method

Before solving the equations of our model, we recast them in a more versatile dimensionless form. Since we have a system of ordinary differential equations with the shock as one boundary, we de-dimensionalize the equations in this section using the properties at the *shock radius*. (Note that this differs from the usual convention of using the virial radius of the underlying dark-matter potential.) We introduce the constants  $R_{\text{sh}}$  and  $M_0$ , which represent the shock radius of the cluster at the present time  $t_0$  and the total mass enclosed within it. (In an isothermal potential,  $R_{\text{sh}}$  and  $M_0$  each differ from the virial radius and mass by a factor of  $2\xi$ .) We also define a dynamical time  $t_{\text{dyn}} \equiv (GM_0/R_{\text{sh}}^3)^{-1/2}$ , along with the spatial coordinate  $x \equiv r/R_{\text{sh}}$  and the Lagrangian mass coordinate  $y \equiv M_b/(f_b M_0)$ .

We introduce the dimensionless gas variables  $P_1$ ,  $\rho_1$ , and  $K_1$  via:

$$\rho_b \equiv \frac{f_b}{4\pi} \frac{M_0}{R_{\text{sh}}^3} \times \rho_1 \quad (5a)$$

$$P \equiv \frac{f_b}{4\pi} \frac{GM_0^2}{R_{\text{sh}}^4} \times P_1 \quad (5b)$$

$$K_1 \equiv P_1/\rho_1^{5/3}. \quad (5c)$$

Thus, the equations for mass conservation and hydrostatic equilibrium become:

$$\frac{dx}{dy} = \frac{(1-\xi)^{4/5}}{3^{3/5}} \left( \frac{t_{\text{dyn}}}{t_0} \right)^{-2/5} \frac{y^{4/5}}{x^2 P_1^{3/5}} \quad (6a)$$

$$\frac{dP_1}{dy} = -\frac{1}{x^3}, \quad (6b)$$

which we solve subject to the boundary conditions at the shock:

$$x(y=1) = 1 \quad (7a)$$

$$P_1(y=1) = \frac{4\sqrt{2}}{3} (1-\xi)^{1/2} \left( \frac{t_{\text{dyn}}}{t_0} \right) \quad (7b)$$

and at the center:

$$x(y=0) = 0. \quad (7c)$$

With these definitions, the solution is independent of the parameters  $f_b$ ,  $\mu$ ,  $R_{\text{sh}}$ , and  $M_0$ . Furthermore, the system is overdetermined with three boundary conditions and two equations. The shock radius  $\xi$  is therefore an eigenvalue which must be chosen to meet the inner boundary condition in equation 7c.

Thus, the *only* free parameter in our system of equations is the ratio  $t_{\text{dyn}}/t_0$ , and we expect to find a one-dimensional family of models. Since the average density of any dark matter halo  $\bar{\rho} \sim 200\rho_{\text{crit}}$  is independent of mass in hierarchical structure formation, we do not expect the dynamical timescale  $t_{\text{dyn}}$  to vary strongly among clusters at any cosmological epoch. The ratio  $t_{\text{dyn}}/t_0$  thus measures the age (or, equivalently, the assembly rate) of the halo.

We note that the following solution to equations 6 and 7:

$$P_1 = \frac{1}{2x^2}, \quad x = y, \quad \xi = \frac{1}{4} \quad (8)$$

exists when the assembly rate satisfies:

$$\frac{t_{\text{dyn}}}{t_0} = \sqrt{\frac{3}{32}}.$$

We describe the physical significance of this special, isothermal solution in section 3.2.

For other values of the assembly rate  $t_{\text{dyn}}/t_0$ , we solve equations 6 and 7 numerically using a predictor-corrector method, and we solve the eigenvalue problem for  $\xi$  with a bisection search. We avoid the singularity in equations 6a and 6b by solving them on a logarithmic grid. Since we cannot apply the boundary condition equation 7c in the logarithmic coordinates, we obtain an approximate boundary condition at a finite radius by expanding the equation for hydrostatic equilibrium near  $x=0$ . Assuming that the temperature remains finite, this equation becomes:

$$T \rightarrow T_{\text{vir}} \left( \frac{d \ln \rho^{-1/2}}{d \ln r} \right)^{-1}.$$

Combined with the fact that  $K \propto T\rho^{-2/3} \propto y^{4/3}$ , this implies that  $\rho \propto r^{-2}$ , and thus that

$$T \rightarrow T_{\text{vir}}, \quad \text{and} \quad (9)$$

$$y \rightarrow \left( \frac{T_{\text{vir}}}{T_{\text{sh}}} \right)^{1/2} \left( \frac{3\rho_{\text{sh}}}{\bar{\rho}} \right)^{1/3} x \quad (10)$$

as  $x \rightarrow 0$ . We use equation 10 as a boundary condition for the eigenvalue problem and equation 9 to check the accuracy of our integration. The analytic solution in equation 8 also permits a more pedantic test of our method.

### 3.2 Results

Figure 1 shows the solution for the dimensionless shock radius  $\xi(t_{\text{dyn}}/t_0)$  from our numerical calculations. In the limit

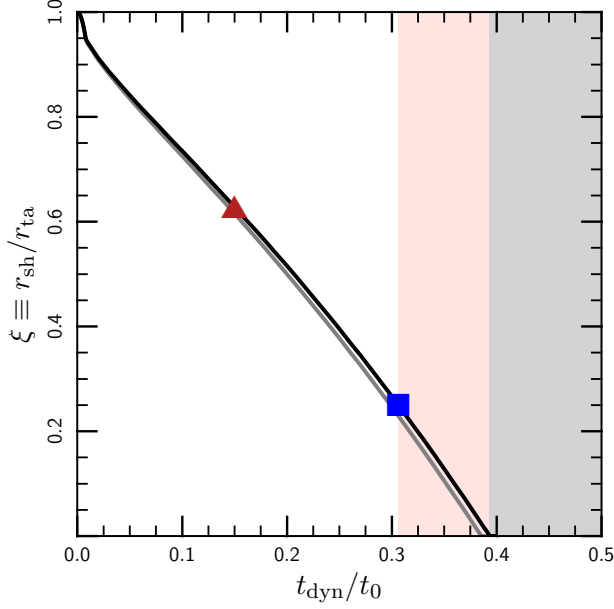


**Figure 1.** Shock radius  $\xi$  as a function of the assembly parameter  $t_{\text{dyn}}/t_0$  for the simplified models described in section 3. The timescale  $t_0 = M/\dot{M}$  is the age of the halo. Points further to the left on this plot correspond to clusters which form slowly and points further to the right correspond to clusters which form rapidly. The red triangle represents the approximate value of  $t_{\text{dyn}}/t_0$  expected for cluster halos. The blue square marks the isothermal solution in equation 8. Clusters in the white region of the plot have negative temperature gradients, clusters in the pink region have positive temperature gradients, and clusters in the gray region cannot exist in our steady-state model. Real clusters are expected to have moderate, negative temperature gradients based on this analysis (see figure 3). The black line illustrates the calculation with an isothermal potential, and the gray line shows results with a more realistic NFW potential.

of very slow accretion (i.e. as  $t_{\text{dyn}}/t_0 \rightarrow 0$ ), the shock is comparatively weak and the dimensionless shock radius  $\xi \rightarrow 1$ . As the assembly rate  $t_{\text{dyn}}/t_0$  increases, the shock radius  $\xi$  decreases monotonically. Thus, the virial shock moves inwards as the accretion rate increases. This result seems intuitively reasonable, as a higher accretion rate implies a higher ram pressure behind the shock. A stronger shock (or smaller  $\xi$ ) is thus required to hold back the infalling material and to keep the ICM in hydrostatic equilibrium.

Interestingly, figure 1 indicates a maximum assembly rate around  $t_{\text{dyn}}/t_0 \approx 0.39$  at which  $\xi \rightarrow 0$ . Beyond this point, thermal pressure alone cannot hold back the accretion shock and hydrostatic equilibrium becomes impossible. This represents an extremely rapid accretion rate, however, with the halo forming over only  $\sim 2.5$  dynamical times; our quasi-static model for the ICM breaks down in this limit. A fully dynamical calculation (e.g. a simulation) with such a high accretion rate would likely produce a model ICM with significant time dependence and turbulent pressure support, but with a finite shock radius.

Figure 1 shows the isothermal solution (eq. 8) as a blue square and a point representative of a massive cluster [with  $t_{\text{dyn}} = 0.1H_0^{-1}$  and  $t_0 \sim (2/3)H_0^{-1}$ ] as a red triangle. Our

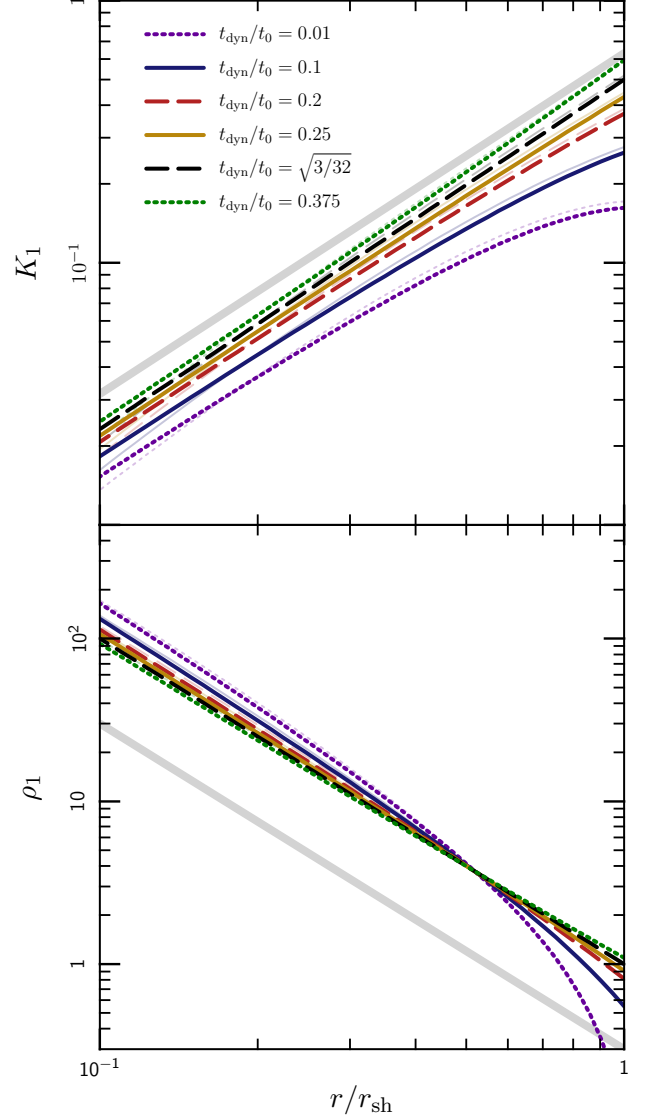


**Figure 2.** Profiles of density and entropy for representative models from fig. 1 with different values of the assembly parameter  $t_{\text{dyn}}/t_0$ . Thick gray lines show typical power-law slopes derived from x-ray observations (Croston et al. 2008; Cavagnolo et al. 2009) (the normalization is arbitrary). Massive clusters should mostly lie between the solid blue and long-dashed red lines. Our solutions are approximately, but not exactly, power-laws. The deviations from power-law behavior are dictated by the outer boundary condition on the pressure and determine the temperature profile (fig. 3). This boundary condition depends on the ram pressure behind the shock, and thus on the speed with which the cluster formed (parametrized by  $t_{\text{dyn}}/t_0$  in this model). As in fig. 1, thick curves show models with simplified, isothermal potentials and thin curves show more realistic models with NFW potentials.

model predicts that  $\xi \sim 0.6$  for this fiducial cluster, similar to what has been expected in the past (e.g. Rees & Ostriker 1977). Note that the isothermal solution requires a much faster assembly than is typical for galaxy clusters; this simple model thus suggests that clusters should not be isothermal.

Figure 1 directly illustrates the effect of the accretion rate on the location of the virial shock. The gas properties in the ICM must match onto jump conditions at the shock;

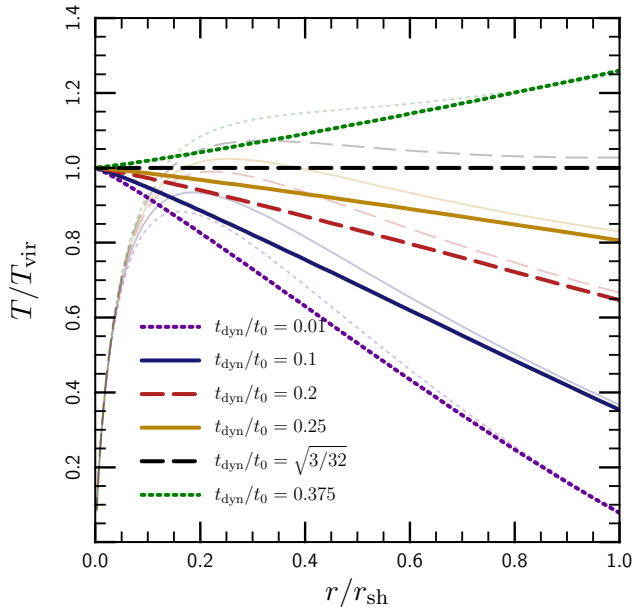


**Figure 3.** Temperature profiles for representative models from fig. 1 with different values of the assembly parameter  $t_{\text{dyn}}/t_0$ . The black line corresponds to the isothermal solution (eq. 8); massive clusters should lie between the blue and red lines. Our model implies temperature profiles which decrease by a factor of  $\sim 2$  from the center to the virial radius, in line with x-ray observations. Thin, light lines show the results of calculations with NFW potentials, rather than isothermal ones (see § 4 for details). The temperature gradients are similar outside the scale radius of the halo.

thus, by moving the shock radius, the accretion rate also influences the thermodynamic structure of the ICM. Figure 2 demonstrates this by showing profiles of the gas density and entropy for models with different assembly rates  $t_{\text{dyn}}/t_0$ . The profiles are nearly isothermal, with  $\rho \sim r^{-2}$  and  $K \sim r^{4/3}$ , and are broadly consistent with determinations from x-ray data (Croston et al. 2008; Cavagnolo et al. 2009).

The small deviations from power-laws in the density and entropy profiles lead to significant temperature gradients, however. We show this explicitly in figure 3, where we plot the temperature profiles for the models from figure 2. The temperature profiles are nearly linear, and gradients of either sign are possible, depending on the assembly rate  $t_{\text{dyn}}/t_0$ . This result is not surprising, since the central temperature must equal the virial temperature of the halo (eq. 9) and the temperature at the shock is dictated by the jump conditions. A roughly linear interpolation between these boundary conditions seems reasonable given the simplicity of the model. The isothermal solution with  $t_{\text{dyn}}/t_0 = \sqrt{3/32}$  divides models with negative and positive temperature gradients. In reality, most clusters satisfy  $t_{\text{dyn}}/t_0 \sim 0.1 - 0.2$ ; in this case our model predicts temperature profiles which decrease by a factor of  $\sim 2$  from the center to the shock radius. This result is in line with recent observations of the gas temperature near the virial radius (George et al. 2009; Simionescu et al. 2011).

Thus, while we solve the system of equations 6a and 6b and boundary conditions 7a–7c for the shock radius and for the structure of the ICM, we find that the boundary conditions essentially dictate the temperature profile. The temper-

ature must reach the virial temperature of the potential at the center of the halo, and it must match onto the jump conditions at the shock. The solution to hydrostatic equilibrium then implies a nearly linear interpolation between these two boundary conditions.

As presented here, the temperature profiles in figure 3 may seem specific to our assumption of an isothermal potential. To demonstrate that this is not the case, we have included calculations with NFW potentials in figure 3 (shown as thin, light lines). Although the different potential has a dramatic effect on the temperature profile within the scale radius, the trend between the assembly rate and the overall temperature gradient at large radii is similar. We include these lines only for illustration, but present much more detailed models with NFW potentials in the following section 4.

The simple model presented in this section suggests that the assembly rate of the halo (or, equivalently, the ram pressure behind the accretion shock) dictates the large-scale temperature gradient in the ICM. The assembly rates of massive clusters are such that they should have moderate, negative temperature gradients outside the scale radius. This is one of our primary findings. In what follows, we show that this result holds true even when we relax the simplifying assumptions in this section. We also study how thermal conduction modifies this ‘baseline’ temperature profile.

## 4 CONDUCTION AND REALISTIC ASSEMBLY HISTORIES

Our models with isothermal potentials and linear accretion histories are especially transparent. The models are very idealized, however, and it is not clear how accurately they carry over to real clusters. In this section, we generalize our results to include more realistic potentials and accretion histories; we also include thermal conduction in our calculation and study its influence on the temperature profiles in clusters.

### 4.1 Method

#### 4.1.1 Coordinates and Assumptions

Introducing realistic potentials and accretion histories into our model necessitates a few changes to our method. Though the unit system introduced in section 3 is ideal for our model equations, the virial mass of the halo (as opposed to the mass enclosed by the virial shock) is an eigenvalue of the problem and cannot be specified ahead of time. Since we want to study the variation in temperature profiles at fixed *virial* mass, we must alter the equations and boundary conditions slightly.

We adopt a unit system based on the virial mass  $M_{\text{vir},0}$  and radius  $r_{\text{vir},0}$  of the halo at redshift zero. Following our approach in the last section, we introduce the dimensionless

variables  $P_1$ ,  $\rho_1$ , and  $K_1$  via:

$$\rho_b \equiv \frac{f_b}{4\pi} \frac{M_{\text{vir},0}}{r_{\text{vir},0}^3} \times \rho_1 \quad (11a)$$

$$P \equiv \frac{f_b}{4\pi} \frac{GM_{\text{vir},0}^2}{r_{\text{vir},0}^4} \times P_1 \quad (11b)$$

$$K_1 \equiv \frac{P_1}{\rho_1^{5/3}}. \quad (11c)$$

We also define the spatial coordinate  $x \equiv r/r_{\text{vir}}$ , the Lagrangian coordinate  $y \equiv M_b/(f_b M_{\text{vir}})$ , and the dynamical time  $t_{\text{dyn}} \equiv (GM_{\text{vir}}/r_{\text{vir}}^3)^{-1/2}$ . Note that our definitions of  $x$ ,  $y$ , and  $t_{\text{dyn}}$  use instantaneous values of  $r_{\text{vir}}$  and  $M_{\text{vir}}$ , while our definitions of  $\rho_1$ ,  $P_1$ , and  $K_1$  are normalized to  $r_{\text{vir},0}$  and  $M_{\text{vir},0}$ . Thermodynamic quantities in our calculation (e.g.  $K_1$ ) are thus directly comparable at different redshifts, while coordinates (e.g.  $x$ ) are not.

We define  $m \equiv M_{\text{vir}}(t)/M_{\text{vir},0}$ , which tracks the formation of the halo and functions as a time coordinate. We take the virial radius to be  $r_{200}$ , the radius within which the mean density of the halo is 200 times the critical density of the universe. Thus,  $t_{\text{dyn}} = (10H)^{-1}$ , where  $H$  is the Hubble parameter.

Since the virial radius does not directly enter into our model (§ 3), our choice defining the virial radius is essentially arbitrary. We chose  $r_{200}$  because it is straightforward to compute and facilitates comparison with much of the existing literature. We continue to use the notation “ $r_{\text{vir}}$ ” over the notation “ $r_{200}$ ” in order to de-emphasize this arbitrary definition, however.

#### 4.1.2 Dark Matter

As discussed in section 2, we do not solve for the evolution of the dark matter; instead, we assume that the dark matter evolves independently of the baryons and we parametrize it using fits to halos from cosmological n-body simulations. In particular, we assume that the dark matter follows an NFW distribution at all times (Navarro et al. 1997), with a constant concentration parameter  $c = 5$ , as is appropriate for actively forming, massive halos (Zhao et al. 2009). The only free parameter in this model for the dark matter is the mass accretion history of the halo.

We use fits to halo mass accretion histories of the form

$$m(z) = [(1+z)^b \exp(-z)]^\gamma, \quad (12)$$

derived by McBride et al. (2009) from the Millennium simulation (Springel et al. 2005). This fit is calibrated to the “friends of friends” mass  $M_{\text{FoF}}$  (Davis et al. 1985), which is similar to our choice of  $M_{200}$  for the virial mass (White 2001). Figure 4 shows the parameter space for the exponents  $\gamma$  and  $b$ , along with the definitions of Type I, II, III, and IV accretion histories from McBride et al. (2009),<sup>3</sup> and figure 5 shows an example of each “Type” of accretion history. For reference,

<sup>3</sup> McBride et al. (2009) do not distinguish between Type II halos with negative and positive values of the exponent  $b$ . Since this distinction is important in our application, we denote Type II halos with  $b < 0$  as Type 0.

the red curves in figure 4 show contours of the probability density function for halo accretion parameters from the appendix of McBride et al. (2009). We also show contours of the “formation redshift”  $z_f$  at which the cluster reaches half its present mass; most of the halos formed at a redshift between 0.5 and 1.

Note that a Type I accretion history is roughly exponential in redshift, which is typical in  $\Lambda$ CDM (Wechsler et al. 2002). At fixed mass, Type 0 halos are younger, while Type II and Type III halos are older, than Type I halos. A Type IV accretion history corresponds to mass loss at late times; this would imply a negative ram pressure at the virial shock in our quasi-equilibrium model. These cases should be studied with fully dynamical, cosmological simulations. Fortunately, at the high masses we wish to study, a relatively small fraction of the total halos exhibit Type IV accretion histories. Moreover, these are systems which have recently undergone major mergers; they are likely to be morphologically disturbed and may be excluded from cosmological samples.

In order to calculate the strength of the virial shock, we require an estimate for the turnaround radius  $r_{\text{ta}}$  (§ 2). Unfortunately, fits to  $r_{\text{ta}}$  from n-body simulations do not seem to be available. Therefore, we simply use the virial theorem to estimate that the turnaround radius is twice the virial radius. The shock radius is then given in terms of the virial radius by  $r_{\text{sh}} = 2\xi r_{\text{vir}}$ . We note that this approximation may overestimate the turn-around radius (cf. Diemand et al. 2007), causing us to predict temperature profiles which are too shallow. This is one of the primary sources of uncertainty in our models.

The quasi-equilibrium model for the dark matter described in this section greatly simplifies our method by eliminating the need to solve for the dark matter dynamics (e.g. by using an n-body simulation or by solving the Jeans equations). This model is ambiguous outside the virial radius, however. Since the virial shock typically lies exterior to the virial radius, it is not a priori clear what value of  $M_{\text{sh}}$  to use in equation 1 for the post-shock entropy. We proceed by presuming that the gas and dark matter first separate at the virial shock; thus, the gravitating mass  $M_{\text{sh}}$  in equation 1 corresponds to the mass  $M_{\text{vir}}$ . After the shock, the gas remains in hydrostatic equilibrium at  $r_{\text{sh}}$  while the dark matter continues to collapse and virializes at the virial radius  $r_{\text{vir}} < r_{\text{sh}}$ . Therefore, when we solve for hydrostatic equilibrium in the post-shocked gas, we assume that the dark matter has relaxed and we extrapolate the NFW profile between the virial and shock radii. This inconsistency in our treatment of the gravitating mass is an unavoidable consequence of applying a quasi-equilibrium model for the dark matter outside the virial radius.

#### 4.1.3 Gas Equations

We solve for the state of the gas using a method very similar to that described in section 3, but we now solve for the shock radius  $\xi(m)$  self-consistently. We discretize the halo formation into the accretion of a finite number of shells and, for each shell  $m_i$ , we solve the full eigenvalue problem for its shock strength  $\xi(m_i)$ . Thus, we simultaneously build up so

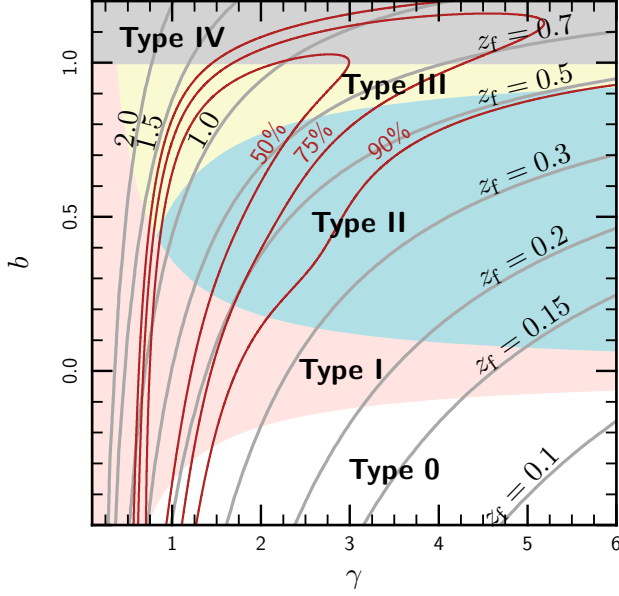


**Figure 4.** Parameter space for dark matter accretion histories based on the Millennium Simulation. The exponents  $\gamma$  and  $b$  are defined in equation 12. Colors demarcate the different accretion “types” from McBride et al. (2009) and gray lines show contours of the formation redshift  $z_f$  such that  $M_{\text{vir}}(z_f) = 0.5 M_{\text{vir}}(z = 0)$ . At redshift zero, Type III halos are accreting very slowly and Type 0 halos are accreting rapidly. The red curves mark contours of the probability density for  $10^{15} M_{\odot}$  clusters to have a given accretion history (taken from the Appendix of McBride et al. 2009). The contours for  $10^{14} M_{\odot}$  halos are very similar to those shown here.

lutions for the shock radius and for the temperature profile as functions of time. As discussed above, we assume that the gas and dark matter first separate at the virial shock. The baryonic accretion rate at the shock radius  $r_{\text{sh}}$  is thus also proportional to equation 12. This is qualitatively consistent with the findings of Faucher-Giguère et al. (2011), who show that the baryonic accretion closely tracks the dark matter accretion history in simulations of high-mass halos.

The equations for mass conservation and hydrostatic equilibrium are:

$$\frac{dx}{dy} = \frac{h^2}{x^2} \left( \frac{K_1(y)}{P_1(y)} \right)^{3/5}, \quad (13a)$$

$$\frac{dP_1}{dy} = -\frac{m^{2/3} h^{8/3}}{x^3} \frac{1}{x} \frac{\log(1+cx) - cx/(1+cx)}{\log(1+c) - c/(1+c)}, \quad (13b)$$

with the boundary conditions:

$$P_1(y=1) = \frac{4\sqrt{2}}{3} m^{2/3} h^{8/3} \eta \sqrt{\frac{1-\xi}{(2\xi)^5}} \quad (14a)$$

$$x(y=1) = 2\xi \quad (14b)$$

$$x(y=0) = 0. \quad (14c)$$

In the above,  $\eta \equiv t_{\text{dyn}}(\partial \ln M_{\text{vir}}/\partial t)$  measures the accretion rate of the halo, and  $h \equiv H/H_0 = [\Omega_m(1+z)^3 + \Omega_\Lambda]^{1/2}$  is the Hubble parameter in units of  $H_0$ . In equations 13 and 14,  $\eta$ ,  $h$ , and  $\xi$  are all evaluated at the epoch of the most recently accreted shell. It is straightforward to show from equation 12

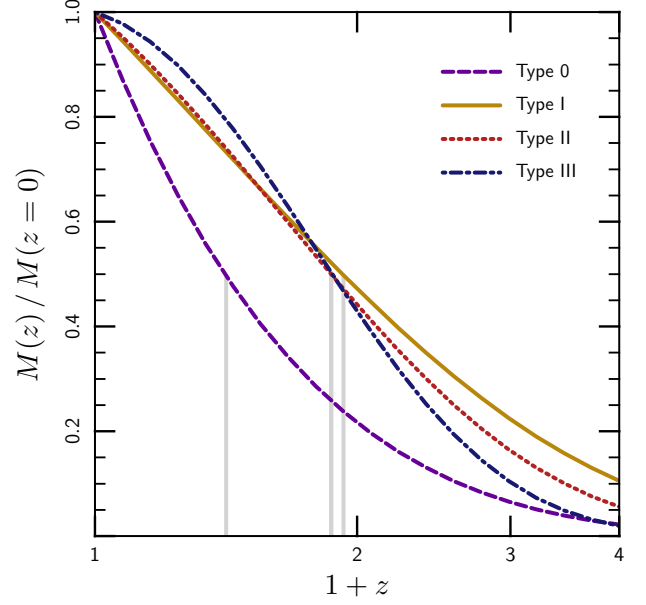


**Figure 5.** Example accretion histories from equation 12 illustrating each of the four “types.” The examples correspond to  $\{\gamma, b\} = \{0.75, -1.5\}$  (Type 0),  $\{0.75, 0.0\}$  (Type I),  $\{1.25, 0.5\}$  (Type II), and  $\{2.25, 0.9\}$  (Type III). These examples are also used in figure 6. Note that Type 0 halos have larger accretion rates, and that Type III halos have lower accretion rates, than intermediate halo types at low redshift. Vertical, gray lines indicate the “formation redshift” for which  $M(z_f) = 0.5 M(z = 0)$ . Though the formation redshift does not have a one-to-one correspondence with accretion type, Type III halos tend to form early and Type 0 halos tend to form late (cf. figure 4).

that  $\dot{m} = m\gamma(1+z-b)H$ . Thus, the dimensionless accretion rate  $\eta$  is given by  $\eta = \gamma(1+z-b)/10$ .

The shock entropy  $K_1^{\text{sh}}$  takes the form:

$$K_1^{\text{sh}}(y) = \frac{1}{3} \left[ \frac{y}{\eta[z(y)] \times h[z(y)]} \right]^{2/3} [1 - \xi(y)]^{4/3}, \quad (15)$$

where  $z(y)$  represents the redshift at which the baryonic shell  $y$  accreted and  $\xi(y)$  represents the shock radius of the cluster at that redshift.

Inserting the conductivity appropriate for a fully-ionized hydrogen plasma (Spitzer 1962) into equation 2 yields:

$$\begin{aligned} \frac{d \ln K_1}{dm} = & 0.70 f_{\text{Sp}} \frac{4\pi \mu^{7/2}}{f_b h m \eta} \left( \frac{M_{\text{vir},0}}{10^{15} M_{\odot}} \right) \\ & \times K_1^{5/2} \left[ \frac{2}{x} \frac{\partial T_1}{\partial x} + \frac{5}{2T_1} \left( \frac{\partial T_1}{\partial x} \right)^2 + \frac{\partial^2 T_1}{\partial x^2} \right]. \end{aligned} \quad (16)$$

(Recall that the coordinate  $m$  tracks the formation of the cluster and thus functions as a time coordinate). We integrate this equation between accretion events with an explicit, sub-cycled method. The conductive heat flux must vanish at the origin by spherical symmetry; thus, we adopt  $\partial T/\partial r = 0$  as the inner boundary condition for equation 16. The precise boundary condition on the heat flux at the shock is uncertain because it depends on the physics of collisionless shocks in the presence of strong thermal conduction. We proceed by



assuming that electrons do not diffuse across the shock into the upstream flow; in our model, the shock thus serves as an insulating boundary. This assumption is convenient because thermal conduction does not modify the structure of the shock. We have also tried calculations in which we keep the heat flux constant at the shock; the results with this alternative boundary condition were very similar to those we present here.

Note that equations 13–15 are independent of halo mass, while equation 16 is not. Conduction thus introduces non-self-similar behavior and may influence mass-observable relations. We quantify this departure from self-similarity in the following section.

The post-shock entropy (eq. 15) and the outer boundary condition on the pressure (eq. 14a) depend on the accretion history through the dimensionless accretion rate  $\eta$  (cf. § 3). Thus, the diversity in accretion histories may generate scatter in the ICM properties at fixed halo mass. In order to estimate the statistics in ICM properties, we generate an ensemble of accretion histories for each halo mass  $M_{\text{vir},0}$ , with the exponents  $\gamma$  and  $b$  drawn from the distribution in the appendix of McBride et al. (2009). This ensemble yields information about the statistics of the cluster population and the extent to which the variation in accretion histories creates scatter in the temperature profile and mass-observable relations. We present these results in the next section.

## 4.2 Results

Before studying the effect of thermal conduction, we present adiabatic models in which we set the effective conductivity to zero. These profiles facilitate comparison with the simpler models in section 3 and also provide a basis for understanding the models with conduction.

Figure 6 shows representative, adiabatic solutions for the redshift-zero temperature profiles resulting from several different accretion histories. (Because we have neglected thermal conduction, these solutions are independent of halo mass.) In all cases, the temperature approaches the virial temperature near the scale radius of the halo, and falls by a factor of  $\sim 2$  by the virial radius. We note that the temperature profiles in figure 6 are not monotonic with density and thus cannot be described with polytropic models. Interestingly, however, a polytrope with an index  $\gamma \sim 1.2$  (as assumed by V03) provides a good fit between the scale radius and  $\sim 0.5 r_{\text{vir}}$ . These profiles are qualitatively very similar to the NFW models in figure 3 with  $t_{\text{dyn}}/t_0 \sim 0.15$ , as is reasonable for clusters (§ 3.2). The location of the accretion shock is also consistent with our interpretation in section 3: Type III halos, which experience slower accretion at late times, have larger shock radii than the more rapidly accreting Type 0 halos. Thus, the intuition we developed in section 3 likely holds even for the more complex models in this section.

Ignoring thermal conduction is not a well-motivated approximation, however: as discussed in section 1, the timescale for heat to diffuse through massive clusters ( $r_{\text{vir}}^2/\chi_e \sim 1$  Gyr) is shorter than the typical age of the ICM ( $\sim 5$  Gyr). Consequently, non-cosmological simulations of isolated halos (e.g. Parrish et al. 2008) show that the ICM becomes almost com-

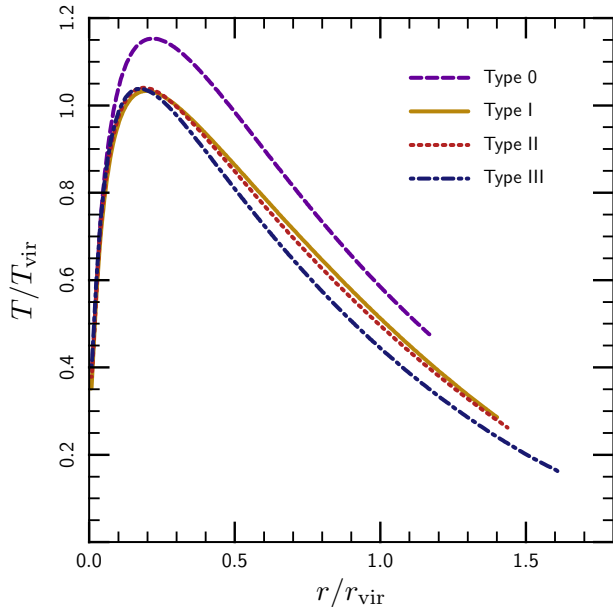
pletely isothermal after  $\sim 2$  Gyr. By analogy, one might therefore expect conduction to significantly modify the temperature profile shown in figures 3 and 6.

Figure 7 compares the temperature profiles of clusters with different effective conductivities. In order to maximize the influence of thermal conduction, we show  $10^{15} M_{\odot}$  clusters (which are hotter, and thus more conductive than lower mass clusters), with Type III accretion histories (which formed comparatively early and thus provide more time for conduction to operate). As expected, thermal conduction smooths out the temperature profile in the ICM; the effect, however, is substantially weaker than has been found in non-cosmological simulations (see above). The profiles we obtain do *not* become isothermal, in qualitative agreement with x-ray observations of the ICM (George et al. 2009; Simionescu et al. 2011), and also with cosmological simulations of clusters which include thermal conduction (Dolag et al. 2004; Burns et al. 2010). The disagreement with simulations of isolated halos suggests that cosmological accretion and the continued formation of clusters is essential not only for understanding the origin of the large-scale temperature gradient in the ICM (§ 3), but also for how this gradient persists in spite of thermal conduction.

Two important effects differentiate cosmological calculations of thermal conduction from non-cosmological simulations of isolated halos. First, even though the present-day timescale for thermal conduction is shorter than the mean age of massive clusters, the gas near the accretion shock is always young and thus unaffected by conduction. The jump conditions at the virial shock therefore still determine the outer temperature, even when we take thermal conduction into account. The second effect differentiating cosmological and non-cosmological calculations is that the ICM at higher redshift had a lower temperature and thus a much lower conductivity than it has at redshift zero. Even at small radii, the age of the ICM ( $\sim 5$  Gyr) thus over-estimates the timescale over which thermal diffusion operates. These two effects, which are not present in non-cosmological simulations, strongly limit the influence of thermal conduction on the large-scale temperature profile of the ICM.

We illustrate these points in figure 8, where for each model from figure 7 we plot the ratio of the age of each shell in the ICM to its field-free conduction timescale. We define the conduction timescale as  $t_{\text{cond}} \equiv |d \ln K / dt|^{-1}$ , calculated using equation 2 with  $f_{\text{Sp}} = 1$ . We define the age of the shell  $t_{\text{age}}$  as the time over which conduction operates at its present-day efficiency; we approximate this as the minimum of the time since the shell accreted and  $|d \ln m / dt|^{-1}$ , the timescale over which the ICM conductivity changes appreciably. Conduction should limit the temperature profile of the ICM to everywhere satisfy  $t_{\text{cond}}/t_{\text{age}} \lesssim f_{\text{Sp}}^{-1}$ . Thus, by looking at the adiabatic models in figure 8 (blue, with  $f_{\text{Sp}} = 0$ ), we can estimate how large of an effect conduction would have if we were to include it.

Figure 8 shows that the ratio  $t_{\text{age}}/t_{\text{cond}}$  falls steeply near the virial shock, again reflecting that the recently accreted gas is too young to be influenced strongly by conduction. At smaller radii, however,  $t_{\text{age}}/t_{\text{cond}} \sim 5$  in the adiabatic model, suggesting that thermal conduction plays a significant role in determining the temperature profile in the ICM. The thin blue



**Figure 6.** Representative temperature profiles at redshift  $z = 0$  generated by each type of accretion history from McBride et al. (2009) (see figures 4 and 5). The profiles are calculated using the Lagrangian method from section 4, but with no thermal conduction (the temperature profiles are thus independent of the halo mass). Note the qualitative agreement with the simple models from section 3. In addition, the location of the shock radius depends fairly sensitively on the accretion history of the halo.

curves in figure 8 show that this conclusion depends strongly on redshift, however. The flattening of the temperature profile shown in figure 7 is thus a fairly recent phenomenon and is far less pronounced at redshift  $z \gtrsim 0.2$ . Recall also that figures 7 and 8 show results for massive,  $10^{15} M_{\odot}$  clusters with Type III accretion histories. Clusters with lower masses or different accretion histories are likely to be even less strongly influenced by conduction (see figure 10, below).

The red and yellow curves in figure 8 show that when we include thermal conduction with a given suppression factor  $f_{\text{Sp}}$ , the temperature gradient adjusts so as to keep the ratio  $t_{\text{cond}}/t_{\text{age}}$  below  $f_{\text{Sp}}^{-1}$ . The ratio  $t_{\text{cond}}/t_{\text{age}}$  is proportional to the gradient term:

$$\left[ \frac{2}{x} \frac{\partial T_1}{\partial x} + \frac{5}{2T_1} \left( \frac{\partial T_1}{\partial x} \right)^2 + \frac{\partial^2 T_1}{\partial x^2} \right].$$

Thus, thermal conduction can either make the ICM isothermal (so that the heat flux vanishes), or make  $T \sim r^{-2/7}$  (so that the heat flux is constant). We find that our model clusters initially take the second approach: the temperature profile adjusts so as to have a nearly constant heat flux as a function of radius. This is not possible near the origin, however, where spherical symmetry requires the heat flux to vanish. Thus, over a longer timescale, the center of the ICM cools and the ICM begins to become isothermal. The yellow curve in figure 7 shows the beginning of this process, but there is not enough time before redshift  $z = 0$  for a significant fraction of the

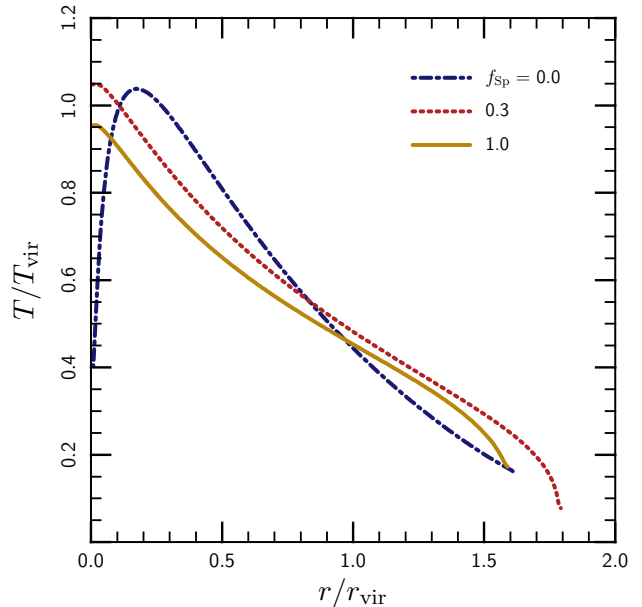


**Figure 7.** Influence of the effective conductivity on cluster temperature profiles. These curves show temperature profiles for massive,  $10^{15} M_{\odot}$  halos with Type III accretion histories at redshift  $z = 0$ . This choice of mass, accretion type, and redshift maximizes the effect of thermal conduction; nonetheless, the change to the temperature profile at large radii is modest. As discussed in the text, the marked effect of thermal conduction on the temperatures at small radii is not a firm prediction, since our models neglect both radiative cooling and feedback heating, which are important in this region (Voit 2011).

ICM to become completely isothermal, even in cases where conduction is most effective.

Though conduction may have considerable effect on the temperature profiles of massive clusters by redshift zero, its influence on their entropy profiles is less pronounced. We show this in figure 9, which compares entropy profiles for massive,  $10^{15} M_{\odot}$  clusters with and without conduction. Between the scale radius and the virial radius, both models agree fairly well with a power-law fit derived from x-ray observations (e.g. Cavagnolo et al. 2009). Interestingly, thermal conduction smooths out some of the non-power-law behavior introduced by the accretion history, leading to an entropy profile more similar to the adiabatic self-similar profile.

Figures 6–9 illustrate the effects of cosmological accretion and thermal conduction on the temperature of the ICM in individual clusters. As mentioned in section 4.1, in order to study the statistics of temperature profiles as a function of virial mass, we run an ensemble of models with accretion histories drawn from the probability distribution in the appendix of McBride et al. (2009). The upper panels of figure 10 show these temperature profiles for three different halo masses with (yellow) and without (blue) thermal conduction. In the models with conduction, we have assumed a conductive suppression factor  $f_{\text{Sp}} = 0.3$ . The temperature profile roughly follows the pattern found in section 3, but with fairly significant,  $\sim 10\%$ , scatter. This scatter is caused purely by the

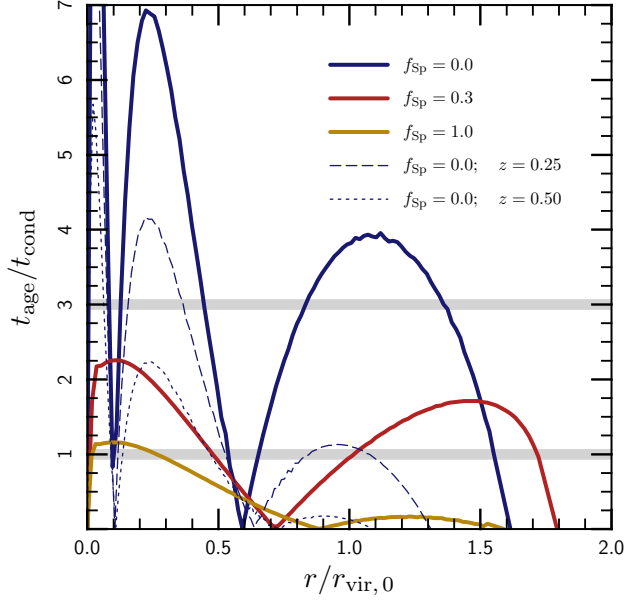


**Figure 8.** Ratio of the age of each shell in the ICM to its field-free conduction timescale (see text for definitions). The models are the same as in figure 7. This ratio is defined using the field-free conductivity (i. e. for  $f_{\text{Sp}} = 1$ ). Models with finite suppression factors should satisfy  $t_{\text{age}}/t_{\text{cond}} \lesssim f_{\text{Sp}}^{-1}$ ; the thick gray lines show this limit for  $f_{\text{Sp}} = 1$  and  $1/3$ . Adiabatic models predict  $t_{\text{cond}} \lesssim (0.2 - 0.3)t_{\text{age}}$  at intermediate radii; as a result, conduction alters the temperature profile and maintains  $t_{\text{age}}/t_{\text{cond}} \lesssim f_{\text{Sp}}^{-1}$ .

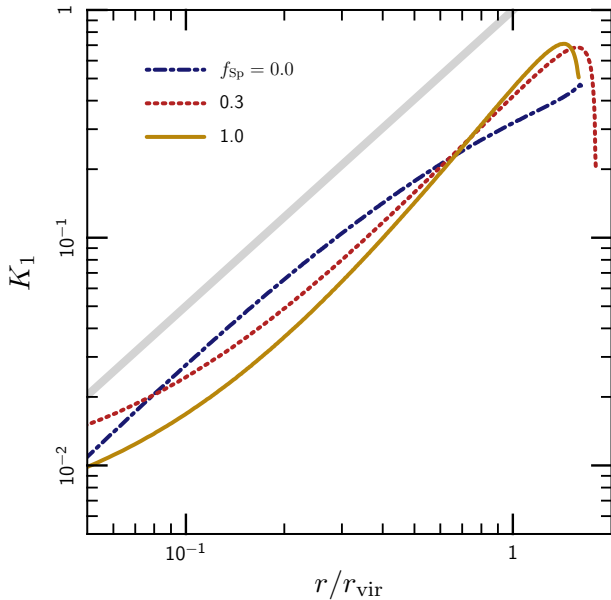


**Figure 9.** Entropy profiles in calculations with different values of the conductivity. As in figure 7, this figure shows  $10^{15} M_{\odot}$  halos with Type III accretion histories; these properties maximize the effect of thermal conduction. Also shown is the  $K \sim r^{1.3}$  power-law derived in V03.

variation in accretion histories.<sup>4</sup> We have neglected several processes, including mergers, heating by dynamical friction, radiative cooling, and heating by AGN outflows, all of which may increase the scatter above that shown here.

Figure 10 also illustrates the mass-dependence of conduction’s role in the ICM. Because the thermal conductivity of a plasma depends sensitively on its temperature as  $\kappa \propto T^{5/2}$ , higher-mass halos are more strongly influenced by conduction. More quantitatively, the conduction timescale in the ICM falls with mass:  $t_{\text{cond}} \sim r_{\text{vir}}^2/\chi_e \sim 1/M_{\text{vir}}$ . Figure 10 shows that the normalization is such that conduction has a minor influence on  $10^{14} M_{\odot}$  halos,<sup>5</sup> but that it is significant for more massive,  $10^{15} M_{\odot}$  clusters.

Finally, in the upper-right panel of figure 10, we have overlaid observational data from Leccardi & Molendi (2008) and Simionescu et al. (2011).<sup>6</sup> The data from Leccardi & Molendi (2008) (shown in black) represent an average temperature profile derived from 48 clusters from the XMM-Newton archive. The points from Simionescu et al. (2011), shown in green, represent SUZAKU observations of the Perseus cluster out to  $r_{200}$ . Outside the scale radius, where our method is applicable, our model agrees favorably with the data. Though this agreement is encouraging, we caution that both the normalization and slope of the data points in this plot are sensitive to the assumed virial mass of the halo, which is uncertain in x-ray observations. Furthermore, several uncertainties in our model, including the turnaround radius, the effect of non-smooth accretion, and deviations from spherical symmetry preclude a very quantitative comparison with the data.

### 4.3 Mixing-Length Theory and the MTI

As an example application of our models, we use mixing-length theory to estimate the turbulent pressure support produced by convection in clusters. In dilute, magnetized plasmas such as the ICM in galaxy clusters, convective stability depends on the temperature gradient of the plasma (Balbus 2001, later generalized by Quataert 2008 and Kunz 2011). This convection, known as the MTI, may produce strong turbulence in clusters (McCourt et al. 2011; Parrish et al. 2012) and thus may provide enough non-thermal pressure support to bias hydrostatic mass estimates of cluster halos. Parrish et al. (2012) found that the convective velocities produced by the MTI roughly obey mixing-length theory. This motivates us to use our model temperature profiles to estimate the turbulent pressure support produced by the MTI as a function of cluster mass and redshift. We note, however, that Kunz

<sup>4</sup> Note that we have neglected any correlation between halo concentration and accretion history, which may introduce additional variation in the temperature profiles (e. g. Bullock et al. 2001). The analysis in Zhao et al. (2009) suggests that a constant value for the concentration  $c \sim 5$  is appropriate for massive clusters, however.

<sup>5</sup> This conclusion applies to the large-scale temperature gradient in the ICM. Of course, small-scale features may be strongly influenced by conduction, even in  $10^{14} M_{\odot}$  halos (cf. Dolag et al. 2004).

<sup>6</sup> The observation presented in George et al. (2009) provides another useful constraint on the properties of the ICM at large radii. We do not include it in figure 10, however, because it is not de-projected and thus not directly comparable to our results.

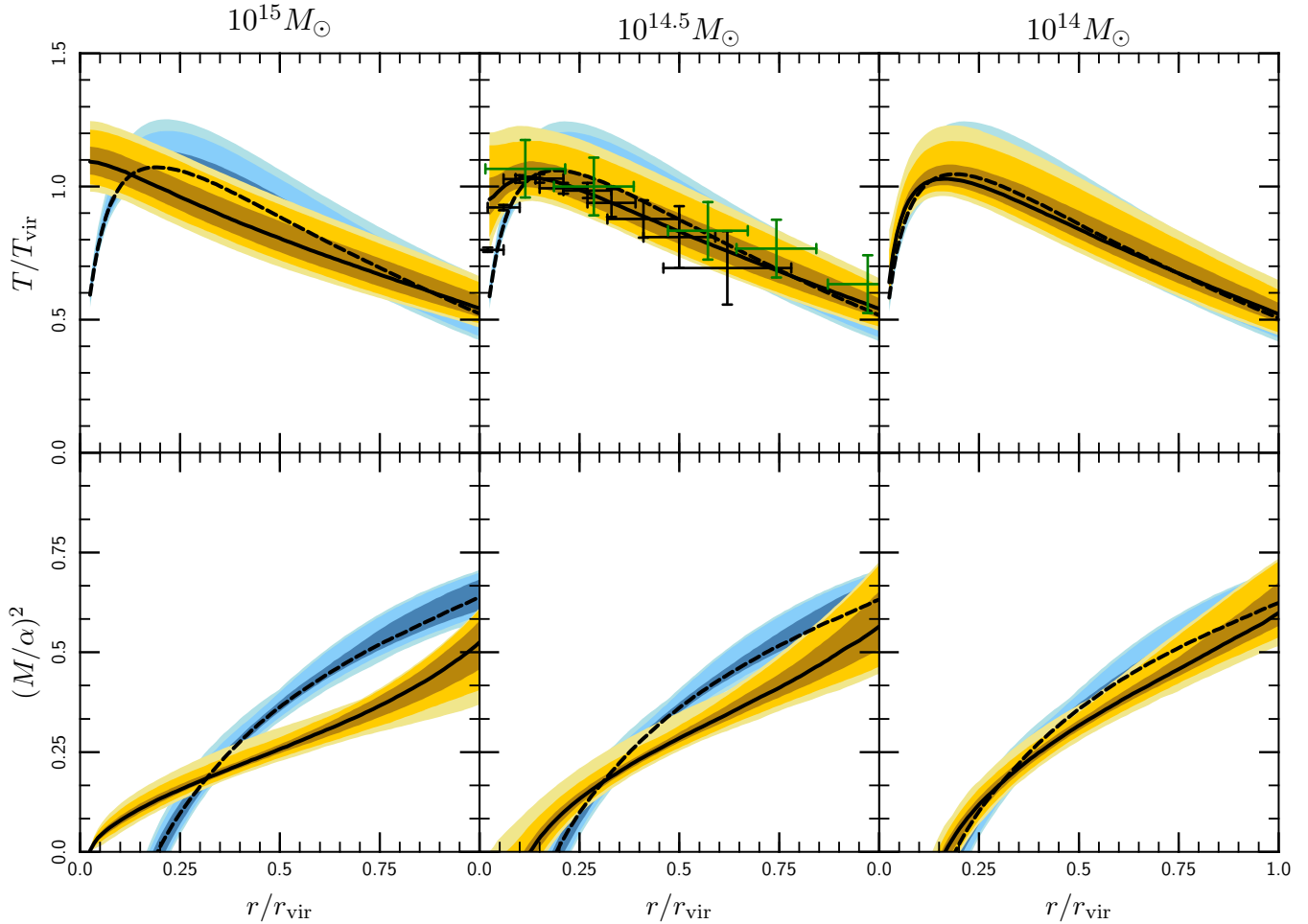


**Figure 10.** (*Top row*): Temperature profiles with (yellow;  $f_{\text{Sp}} = 0.3$ ) and without (blue) thermal conduction for different halo masses. Black lines show the median profile from our ensemble of accretion histories based on figure 4 and colors show contours enclosing 50%, 90%, and 99% of the models. The points with error bars in the top-right panel show temperature profiles derived from x-ray observations. The black and green points are taken from Leccardi & Molendi (2008) and Simionescu et al. (2011), respectively. (*Bottom row*): Estimated fraction of non-thermal pressure support generated by the MTI. See section 4.3 for details.

et al. (2012) have shown that the strength of this turbulence depends on the magnetic field strength in the ICM, an effect which we do not account for in our simple estimates.

Assuming that the convective motions retain their coherence for a fraction  $\alpha$  of a pressure scale-height and that magnetic tension does not suppress the convective motions, we expect the instability to drive turbulent convection with Mach numbers of order:

$$M \sim \alpha \left( H \frac{d \ln T}{dr} \right)^{1/2}, \quad (17)$$

where  $H \equiv (d \ln P / dr)^{-1}$  is the pressure scale-height. The bottom panels of figure 10 show this estimate for the turbulent pressure support (proportional to  $M^2$ ). Assuming (as suggested by the simulations in Parrish et al. 2012) that the mixing length parameter  $\alpha \sim 0.5$ , this figure suggests that turbulence driven by the MTI contributes  $\sim 5 - 10\%$  of the pressure support outside of  $r_{500}$ . Cosmological simulations of cluster formation (e.g. Rasia et al. 2006; Nagai et al. 2007; Vazza et al. 2011) find significant turbulent pressure support due to subsonic, bulk flows driven by mergers near the virial

radius. We note that any turbulence produced by the MTI would add to, but would likely be sub-dominant to, that produced by infalling subhalos.

Since the MTI is not suppressed by other sources of turbulence (McCourt et al. 2011; Parrish et al. 2012), this pressure support adds to that already present due to turbulence driven by infalling substructure or by galaxy wakes. This analysis suggests that the MTI plays an important role in the dynamics of the ICM, especially at radii  $\gtrsim 0.5 r_{\text{vir}}$ . Thus, the MTI may provide an interesting correction for hydrostatic mass estimates of cluster halos. Unfortunately, both the large scatter in the strength of the MTI and its strong radial dependence (cf. Parrish et al. 2012) seem to preclude a simple fitting function for the fraction of turbulent pressure support as a function of halo mass.

By applying mixing-length theory in equation 17, we have implicitly assumed that the MTI grows rapidly enough to establish convection by redshift zero. We find that  $t_{\text{MTI}} \lesssim 0.5 t_{\text{age}}$  within  $r_{\text{vir}}$ ; thus, the Mach numbers in figure 10 (and

also in Parrish et al. 2012) are likely to be reasonable estimates.

Another assumption implicit in our use of mixing-length theory is that conduction is rapid enough to sustain the MTI. Thus, the results in the lower panels of figure 10 are only valid when the conduction timescale across an unstable mode  $\sim (\alpha H)^2/\chi$  is less than the growth time of the MTI. Massive clusters ( $M_{\text{vir}} \gtrsim 10^{14.5} M_{\odot}$ ), likely satisfy this ordering of timescales, but lower masses halos ( $M_{\text{vir}} \lesssim 10^{14} M_{\odot}$ ) may not. Thus, the mass-dependence of the MTI is not likely to be monotonic. In the most massive halos ( $M_{\text{vir}} \gtrsim 10^{15} M_{\odot}$ ), thermal conduction is more efficient and weakens the temperature gradient at intermediate radii (fig. 10). In lower mass halos ( $M_{\text{vir}} \lesssim 10^{14} M_{\odot}$ ), on the other hand, conduction may not be fast enough to drive the MTI to its full potential. This analysis suggests that  $10^{14.5} M_{\odot}$  halos experience the most vigorous convection driven by the MTI.

## 5 DISCUSSION

This paper provides a simplified, spherically symmetric model for the temperature profiles of the hot plasma in galaxy groups and clusters. Our model is similar in spirit to earlier studies of the entropy profiles in clusters (e.g. Tozzi & Norman 2001; Voit et al. 2003), but builds on these earlier studies by focusing on temperature and by including the effects of thermal conduction. Our results agree reasonably well with the profiles derived from x-ray observations (cf. Leccardi & Molendi 2008) and from numerical simulations (e.g. Dolag et al. 2004).

We have shown that the large-scale temperature gradient in the ICM is primarily determined by the accretion history of its halo: while the gas near the center of a cluster reaches the virial temperature of the halo, the temperature at the virial shock is determined by the ram pressure of the accreting gas. This difference sets the overall shape of the temperature profile. The timescale for thermal conduction ( $t_{\text{cond}} \sim r_{\text{vir}}^2/\chi_e$ ) is somewhat shorter than the age of the ICM. However, the influence of thermal conduction on the global temperature profile in clusters is mitigated for two reasons. The gas near the center of the cluster is less strongly effected by conduction because it was cooler in the relatively recent past. The gas near the virial shock, on the other hand, has only recently accreted and is younger than the conduction timescale. Thus, conduction has a diminished effect both near the center of the cluster and near the outskirts. As a result, it does not dramatically change the mean temperature profile (fig. 10). Of course, conduction can have a dramatic effect on small-scale inhomogeneities in the ICM (cf. Dolag et al. 2004); such inhomogeneities cannot be studied in our one-dimensional model.

Our results demonstrate the close relationship between the temperature gradient in clusters and the cosmological evolution of the host halo. This implies that numerical studies of isolated cluster models (e.g. Parrish et al. 2008) cannot correctly predict the evolution of the large-scale temperature profile, though they are very useful for studying other aspects of the ICM, such as the interplay among cooling, feedback, and plasma instabilities within the scale radius of the halo.

One of our motivations for studying the effects of conduction and halo accretion history on temperature gradients in clusters is that the free energy in the non-zero temperature gradient drives an efficient convective instability, the MTI. The results in section 4.3 (e.g. fig. 10) show that the turbulent pressure support generated by the MTI may be of order  $\sim 5$  percent of the thermal pressure, and that it scales non-monotonically with halo mass. The magnitude of the turbulent pressure support is sensitive to the accretion history and does not seem amenable to a simple fitting formula.

Halo accretion histories have been studied extensively with numerical simulations. We use the fits to the Millennium simulation from McBride et al. (2009) to estimate the scatter in temperature profiles as a function of halo mass; at redshift  $z = 0$ , this scatter is of order 10%. This scatter likely contributes to the dispersion in cluster mass-observable relations relevant to x-ray and SZ observations. Perhaps more interesting are the effects of thermal conduction and convection, which introduce systematic changes to the temperature profile with mass. In particular, conduction smooths out the temperature profile (and decreases the peak temperature in the halo) by an amount that increases monotonically with halo mass (fig. 10); convection, on the other hand, produces turbulent pressure support that is non-monotonic in halo mass, peaking around  $10^{14.5} M_{\odot}$  halos (§ 4.3).

Figures 6, 7, and 10 demonstrate that the effect of thermal conduction on a cluster's temperature profile is at least as large as the differences produced by normal variation in accretion histories. Any variation in the factor  $f_{\text{sp}}$  (which parameterizes the suppression of the effective radial thermal conductivity relative to the field-free value), if it exists, would create additional scatter in the temperature profiles at fixed mass. Possible effects influencing  $f_{\text{sp}}$  include magnetic draping around infalling or orbiting substructure (Dursi & Pfrommer 2008; Pfrommer & Dursi 2010) and the strength of the magnetic field. These processes may also contribute to the scatter in cluster mass-observable relations.

The models presented in this paper provide a simple explanation for the physics that sets the temperature profiles in galaxy groups and clusters at large radii. Our results are consistent with current observational constraints on cluster temperature profiles at large radii (fig. 10). They also highlight several processes which may bias hydrostatic mass estimates of clusters, including modifications to the scaling relation  $T(M)$  by conduction and by turbulence driven by the MTI. The approximations in this paper, especially the assumptions of smooth accretion and spherical symmetry, preclude precise estimates of the non-thermal pressure support produced by the MTI. These limitations can be addressed using cosmological simulations.

## ACKNOWLEDGMENTS

E. Q., I. P., and M. M. were partially supported by NASA ATP grant NNX10AC95G, Chandra theory grant TM2-13004X, and a Simons Investigator award from the Simons Foundation to EQ. We are grateful to Chung-Pei Ma, James McBride, and Claude-André Faucher-Giguère for helpful

discussions about the structure of dark-matter halos and their mass accretion histories. We also thank Mark Voit for pointing out applications of the  $T(M)$  relationship, and we thank the anonymous referee for suggesting several improvements to the original manuscript. We made our figures using the open-source program TIOGA. This research has made extensive use of NASA's Astrophysics Data System.

## REFERENCES

- Allen, S. W., Evrard, A. E., & Mantz, A. B. 2011, *Annual Reviews of Astronomy and Astrophysics*, 49, 409
- Allen, S. W., Rapetti, D. A., Schmidt, R. W., et al. 2008, *Monthly Notices of the Royal Astronomical Society*, 383, 879
- Balbus, S. A. 2001, *Astrophysical Journal*, 562, 909
- Bullock, J. S., Kolatt, T. S., Sigad, Y., et al. 2001, *Monthly Notices of the Royal Astronomical Society*, 321, 559
- Burns, J. O., Skillman, S. W., & O'Shea, B. W. 2010, *Astrophysical Journal*, 721, 1105
- Cavagnolo, K. W., Donahue, M., Voit, G. M., & Sun, M. 2009, *Astrophysical Journal Supplement*, 182, 12
- Croston, J. H., Pratt, G. W., Böhringer, H., et al. 2008, *Astronomy and Astrophysics*, 487, 431
- Davis, M., Efstathiou, G., Frenk, C. S., & White, S. D. M. 1985, *Astrophysical Journal*, 292, 371
- Diemand, J., Kuhlen, M., & Madau, P. 2007, *Astrophysical Journal*, 667, 859
- Dolag, K., Jubelgas, M., Springel, V., Borgani, S., & Rasia, E. 2004, *Astrophysical Journal Letters*, 606, L97
- Dursi, L. J. & Pfrommer, C. 2008, *Astrophysical Journal*, 677, 993
- Faucher-Giguère, C.-A., Kereš, D., & Ma, C.-P. 2011, *Monthly Notices of the Royal Astronomical Society*, 417, 2982
- Fox, D. C. & Loeb, A. 1997, *Astrophysical Journal*, 491, 459
- George, M. R., Fabian, A. C., Sanders, J. S., Young, A. J., & Russell, H. R. 2009, *Monthly Notices of the Royal Astronomical Society*, 395, 657
- Gunn, J. E. & Gott, III, J. R. 1972, *Astrophysical Journal*, 176, 1
- Komatsu, E. & Seljak, U. 2001, *Monthly Notices of the Royal Astronomical Society*, 327, 1353
- Kunz, M. W. 2011, *Monthly Notices of the Royal Astronomical Society*, 417, 602
- Kunz, M. W., Bogdanović, T., Reynolds, C. S., & Stone, J. M. 2012, *Astrophysical Journal*, 754, 122
- Lau, E. T., Kravtsov, A. V., & Nagai, D. 2009, *Astrophysical Journal*, 705, 1129
- Leccardi, A. & Molendi, S. 2008, *Astronomy and Astrophysics*, 486, 359
- McBride, J., Fakhouri, O., & Ma, C.-P. 2009, *Monthly Notices of the Royal Astronomical Society*, 398, 1858
- McCourt, M., Parrish, I. J., Sharma, P., & Quataert, E. 2011, *Monthly Notices of the Royal Astronomical Society*, 413, 1295
- McCourt, M., Sharma, P., Quataert, E., & Parrish, I. J. 2012, *Monthly Notices of the Royal Astronomical Society*, 419, 3319
- Nagai, D., Vikhlinin, A., & Kravtsov, A. V. 2007, *Astrophysical Journal*, 655, 98
- Narayan, R. & Medvedev, M. V. 2001, *Astrophysical Journal Letters*, 562, L129
- Navarro, J. F., Frenk, C. S., & White, S. D. M. 1997, *Astrophysical Journal*, 490, 493
- Parrish, I. J., McCourt, M., Quataert, E., & Sharma, P. 2012, *Monthly Notices of the Royal Astronomical Society*, 419, L29
- Parrish, I. J., Stone, J. M., & Lemaster, N. 2008, *Astrophysical Journal*, 688, 905
- Pfrommer, C. & Dursi, L. J. 2010, *Nature Physics*, 6, 520
- Quataert, E. 2008, *Astrophysical Journal*, 673, 758
- Rasia, E., Ettori, S., Moscardini, L., et al. 2006, *Monthly Notices of the Royal Astronomical Society*, 369, 2013
- Rees, M. J. & Ostriker, J. P. 1977, *Monthly Notices of the Royal Astronomical Society*, 179, 541
- Rudd, D. H. & Nagai, D. 2009, *Astrophysical Journal Letters*, 701, L16
- Ruszkowski, M., Lee, D., Brüggén, M., Parrish, I., & Oh, S. P. 2011, *Astrophysical Journal*, 740, 81
- Sharma, P., McCourt, M., Quataert, E., & Parrish, I. J. 2012, *Monthly Notices of the Royal Astronomical Society*, 420, 3174
- Sharma, P., Parrish, I. J., & Quataert, E. 2010, *Astrophysical Journal*, 720, 652
- Shaw, L. D., Nagai, D., Bhattacharya, S., & Lau, E. T. 2010, *Astrophysical Journal*, 725, 1452
- Simionescu, A., Allen, S. W., Mantz, A., et al. 2011, *Science*, 331, 1576
- Spitzer, L. 1962, *Physics of Fully Ionized Gases* (John Wiley & Sons Inc.)
- Springel, V., White, S. D. M., Jenkins, A., et al. 2005, *Nature*, 435, 629
- Tozzi, P. & Norman, C. 2001, *Astrophysical Journal*, 546, 63
- Vazza, F., Brunetti, G., Gheller, C., Brunino, R., & Brüggén, M. 2011, *Astronomy and Astrophysics*, 529, A17
- Voit, G. M. 2011, *Astrophysical Journal*, 740, 28
- Voit, G. M., Balogh, M. L., Bower, R. G., Lacey, C. G., & Bryan, G. L. 2003, *Astrophysical Journal*, 593, 272
- Voit, G. M. & Ponman, T. J. 2003, *Astrophysical Journal Letters*, 594, L75
- Wechsler, R. H., Bullock, J. S., Primack, J. R., Kravtsov, A. V., & Dekel, A. 2002, *Astrophysical Journal*, 568, 52
- White, M. 2001, *Astronomy and Astrophysics*, 367, 27
- Zhao, D. H., Jing, Y. P., Mo, H. J., & Börner, G. 2009, *Astrophysical Journal*, 707, 354